Journal of
Biomedical Optics

SPIEDigitalLibrary.org/jbo

# On-chip digital microfluidic architectures for enhanced actuation and sensing

Jacqueline Nichols
Christopher M. Collier
Emily L. Landry
Michael Wiltshire
Brandon Born
Jonathan F. Holzman

SPIE

Journal of Biomedical Optics 17(6), 067005 (June 2012)

# On-chip digital microfluidic architectures for enhanced actuation and sensing

**Jacqueline Nichols, Christopher M. Collier, Emily L. Landry, Michael Wiltshire, Brandon Born, and Jonathan F. Holzman**
University of British Columbia, 3333 University Way, Kelowna, British Columbia, V1V1V7, Canada

**Abstract.** An on-chip system is presented with integrated architectures for digital microfluidic actuation and sensing. Localized actuation is brought about by a digital microfluidic multiplexer layout that overcomes the challenges of multi-microdrop interference, and complete two-dimensional motion is shown for microdrops on a $14 \times 14$ grid with minimized complexity by way of $14 + 14$ inputs. At the same time, microdrop sensing is demonstrated in a folded-cavity design for enhanced optical intensity probing of internal fluid refractive indices. The heightened intensities from this on-chip refractometer are shown to have a linear response to the underlying fluid refractive index. An electro-dispensing technique is used to fabricate the folded-cavity optical architecture in a format that is tuned for the desired refractive index range and sensitivity. The overall lab-on-a-chip system is successful in integrating localized microdrop actuation and sensing. [DOI: 10.1117/1.JBO.17.6.067005]

Keywords: digital microfluidic device; lab-on-a-chip; electrowetting; refractometry; optical sensing; integrated optics.

Paper 12048 received Jan. 23, 2012; revised manuscript received Apr. 4, 2012; accepted for publication May 8, 2012; published online Jun. 11, 2012.

## 1 Introduction

Microfluidic systems have great potential for high-sensitivity analytical processing in biotechnology, physiochemical, and environmental applications.[1,2] The miniaturization of these microsystems has led to continued improvements in performance and throughput by corresponding decreases in both analysis times and reagent volumes.[3] Continuous flow microfluidic structures have been the standard format for implementing such integrated systems, with micromachined channels, valves and pumps executing desired fluid flow control in application-specific lab-on-a-chip devices.[4,5]

For many contemporary analytical technologies there exists a desire for reconfigurability or even real-time adaptive processing—features that are not compatible with permanently etched or micromachined fluid flow structures. In response, digital microfluidics has emerged to meet these adaptability requirements.[6–8] Digital microfluidic systems employ programmable voltage-induced actuation of discrete fluid microdrops with independent control applied over a two-dimensional (2-D) electrode plane (ideally). The generalized nature of this digital architecture, along with the adaptability of the voltage-induced electrohydrodynamic actuation process,[9] makes such a reconfigurable system highly advantageous. The 2-D layout can be programmed for user-defined analytical tasks, while adaptive control can be implemented to provide real-time fault detection, path planning, and process scheduling.[10] Comprehensive details on digital microfluidics can be found in the work of Berthier[11] and a recent review by Jebrail and Wheeler.[12]

A primary challenge for 2-D digital microfluidics relates to actuation scalability—defined here as the need for complete 2-D fluid actuation with fine spatial resolutions and numerous inputs. Generalized actuation is achieved with digital microfluidic structures incorporating 2-D square-electrode grids with $M$ rows and $N$ columns. This becomes impractical in large grids, though, as $M \times N$ input electrical address lines are needed to apply voltages to all $M \times N$ electrodes without overlapping, crossing or shorting address lines. Such 2-D grids have been restricted, therefore, to sizes on the order of $2 \times 4$.[13] (Multilevel topologies with electrical via holes[14] are typically avoided due to their increased fabrication costs and photolithographic complexity.) Ideally, one must ease electrical addressability constraints and reduce system inputs to facilitate actuation in complex digital microfluidic architectures. Section 2 of this work builds upon our prior digital microfluidic multiplexer[15] to ease these addressability constraints by way of a bi-layered linear electrode structure incorporating lower rows and upper columns. This system can actuate microdrops at all $M \times N = 14 \times 14 = 196$ grid locations with only $M + N = 14 + 14 = 28$ electrical inputs through differential voltage biasing with AC voltage waveforms on the upper and lower electrodes having opposite polarities. The design presented here is adapted for practical operation at a 0.64 $V_{\mathrm{rms}}$ level—being well below the 5 V limit for the ultimate application to transistor-transistor logic (TTL) and low-voltage CMOS technologies.[16]

A secondary challenge for 2-D digital microfluidics relates to sensing scalability—defined here as the need for probing fluid state information with enhanced sensitivity. The trend toward lower reagent volumes in smaller grid locations sacrifices measurement sensitivity, as signal levels associated with standard optical transmission/reflection[17] and capacitance sensing[18] scale down with the sampling area. On-chip analyses, such as optical refractometry,[19] can thus have unacceptably low sampling areas and sensitivity. Ideally, one must improve sensing capabilities for localized sampling in complex digital microfluidic

---

Address all correspondence to: Jonathan F. Holzman, The University of British Columbia, 3333 University Way, Kelowna, BC, V1V1V7, Canada. Tel: +2508078798; Fax: +2508079850; E-mail: jonathan.holzman@ubc.ca.

architectures, and a folded-cavity optical refractometry element is introduced in this work as a dedicated refractive index sampling station. The folded-cavity refractometer uses the bi-layer digital microfluidic multiplexer structure with an overhead microlens to form a back-reflected optical internal fluid monitor. It is shown that such refractive index interrogation can be carried out over narrow or wide refractive index ranges, with high or low measurement sensitivities, respectively, according to the designed microlens contact angle. Our established electro-dispensing fabrication process[20] is adapted for use in this folded-cavity refractometer, to facilitate the in-situ microlens contact angle tuning and ultimately enable sensing with the desired refractive index range and sensitivity.

## 2 Actuation

Digital microfluidic devices employ distributed electrode structures to create spatial voltage distributions and actuate internal fluids. The generalized electrode geometry for accomplishing this is the 2-D square electrode grid structure.[21,22] Such a system offers complete microdrop control at all $M \times N$ grid locations, but suffers from addressability issues when scaled to large $M$ and $N$ values. All $M \times N$ electrical input lines must be routed from off-chip contact pads to internal electrodes between electrode gaps in the 2-D plane, and such address lines can become unwieldy to implement without crossing, overlapping or shorting.

To enhance actuation and ease 2-D digital microfluidic addressability constraints, an innovative cross-referenced structure was introduced by Xiao et al.[23] The cross-referenced structure uses orthogonal and separated upper and lower linear electrode arrays, thus 2-D horizontal and vertical microdrop motion can be induced between these upper and lower electrodes. This technique can be scaled for use with a large $M \times N$ grid, as the linear electrodes act as both the actuation electrodes and addressing lines, and only $M + N$ inputs are needed. Unfortunately, the reduction of inputs can lead to the multi-microdrop interference phenomenon when multiple microdrops are present. The applied upper and lower electrode voltages needed to move one microdrop could inadvertently actuate other microdrops along the activated electrodes. Path planning,[10] routing,[24] and graph theory scheduling[25] have all been proposed to alleviate this multi-microdrop interference effect.

In this work, the cross-referenced layout is extended for use with low-voltage differential AC voltage biasing. The resulting digital microfluidic multiplexer gives complete $M \times N$ addressability in the 2-D on-chip plane with only $M + N$ inputs and no observable multi-microdrop interference. Positive and negative voltage polarities are applied via phase-shifts to lower and upper electrodes, respectively, establishing a trinary input state of differential voltage amplitudes between the upper and lower electrodes on the 2-D grid: (1) Grid locations along unactivated upper or lower electrodes are grounded; (2) Grid locations along activated upper or lower electrodes, excluding activated electrode crosspoints, have a differential voltage equal to the applied voltage amplitude; (3) Activated electrode crosspoints have a differential voltage equal to twice the applied voltage amplitude. This trinary state of differential voltages can then be used in tandem with the well-known threshold voltage phenomenon[26] to initiate motion of a single microdrop in the 2-D plane at the activated electrode crosspoint. The applied voltage is selected to be less than the threshold voltage and greater than one-half the threshold voltage to allow only this doubled-voltage crosspoint to overcome the threshold.

Threshold-based differential actuation can be implemented in a practical design through the use of voltage-transformed AC waveforms. Microdrop motion occurs at lower voltages for AC waveforms, and the low current draw through insulating device layers allows for especially low input voltages, $V_{\mathrm{in}}(0\ \mathrm{deg})$, on the primary side of the voltage step-up transformer. To form out-of-phase AC voltage waveforms for the differential voltage actuation technique, a center-tap transformer is used. The resulting AC-actuated digital microfluidic multiplexer is shown in Fig. 1. Positive-polarity waveforms defined by $V_0(0\ \mathrm{deg})$ are directed from the secondary side of the transformer to the desired $i$'th lower electrode row with an $i$-phase-switch, while negative-polarity waveforms defined by $V_0(180\ \mathrm{deg})$ are directed from the secondary side of the transformer to the $j$'th upper electrode column with a $j$-phase-switch. The applied voltage amplitude $V_0$ is linked to the threshold voltage $V_{\mathrm{th}}$ through the inequality $V_{\mathrm{th}}/2 < V_0 < V_{\mathrm{th}}$. A $V_0$ value in this range will initiate microdrop motion only at the one desired activated electrode crosspoint.

To quantify the microdrop motion with activation the $i$'th lower row electrode and $j$'th upper column electrode, it is necessary to link the differential voltage $V_{ij}$ at the $(i, j)$ crosspoint to the local modified fluid surface tension $\Delta\gamma$ with[27]

$$\Delta\gamma = \frac{1}{2} c \begin{cases} V_{ij}^2 - V_{\mathrm{th}}^2, & V_{ij} > V_{\mathrm{th}} \\ 0 & V_{ij} \le V_{\mathrm{th}} \end{cases}, \tag{1}$$

where $c$ is the capacitance per unit area. For a small differential voltage, $V_{ij} \le V_{\mathrm{th}}$, there is insufficient electric field to induce microdrop motion; for a larger differential voltage, $V_{ij} > V_{\mathrm{th}}$, the local electric field creates a non-zero modified surface tension, $\Delta\gamma$, inducing the desired microdrop motion. Such actuation localization is apparent from a comparison of the fluid's modified surface tension distribution in a system with negligible

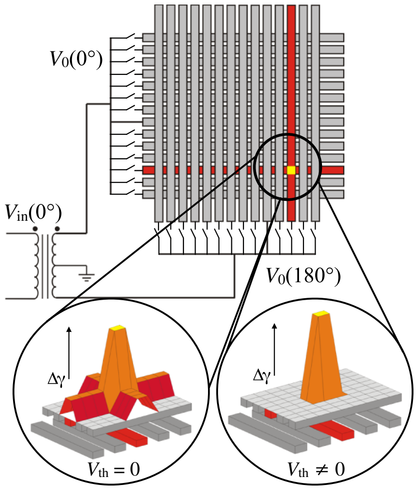

**Fig. 1** The digital microfluidic multiplexer is shown as an orthogonal grid of lower row electrodes and upper column electrodes driven by a center-tap transformer with a single primary input, $V_{\mathrm{in}}(0\ \mathrm{deg})$, and two out-of-phase secondary outputs, $V_0(0\ \mathrm{deg})$ and $V_0(180\ \mathrm{deg})$. For $V_{\mathrm{th}} = 0$, the modified fluid surface tension $\Delta\gamma$ in the left figure inset can allow microdrop motion along all activated row and column electrodes. For $V_{\mathrm{th}} \neq 0$, the modified fluid surface tension in the right figure inset can allow microdrop motion at a single desired activated electrode crosspoint.

threshold voltage, $V_{\text{th}} = 0$ (Fig. 1, left inset), and a system with finite threshold voltage, $V_{\text{th}} \neq 0$ (Fig. 1, right inset). Note that there exists the possibility for motion along all activated electrodes in the left inset, while the possibility for motion is localized to the activated electrode crosspoint in the right inset. The enhanced localization brought about by this multiplexing technique can greatly enhance the scalability of the actuation process and will be used in this work for 2-D microdrop control on a $14 \times 14$ grid.

Microdrop actuation is tested in the afore-mentioned bi-layer digital microfluidic multiplexer. The structure consists of two silica plates with 50-nm thick copper electrodes. Copper features are patterned onto the silica plates via UV photolithography to produce a digital microfluidic multiplexer with 14 linear electrodes having $w = 500\ \mu$m width and $p = 600\ \mu$m centre-to-centre pitch. This pitch sets a fundamental lower limit on the microdrop diameter and can be readily reduced in this linear electrode structure if operation is desired for smaller microdrop diameters. For operation wishing to avoid mixing between multiple microdrops, the relevant microdrops should be separated by a distance of at least this electrode pitch.[28] Each plate is spin-coated with a layer of polydimethylsiloxane (PDMS) followed by a layer of Teflon AF. After high-temperature curing, the electrode plates are aligned in the orthogonal form of Fig. 1 with a separated plate distance of $d = 650\ \mu$m. Fluid motion in the digital microfluidic multiplexer is tracked by an overhead high-resolution camera and apochromatic microscope (LEICA APOZ6).

Voltage biasing is applied to the digital microfluidic multiplexer at 470 Hz as two opposite-phase AC waveforms. The waveforms are generated by a center-tap transformer (Hammond 117E4) having a voltage gain of $2V_0/V_{\text{in}} = 75$ between the opposite-polarity secondary terminals and the input. The positive-polarity secondary-side waveform $V_0(0\ \text{deg})$ is directed to the $i$'th lower electrode row with a $i$-phase-switch; the negative-polarity secondary-side waveform $V_0(180\ \text{deg})$ is directed to the $j$'th upper electrode row with a $j$-phase-switch.

Initial digital microfluidic multiplexer tests are carried out for a device with thick (10 $\mu$m) PDMS layers and a correspondingly high threshold voltage, $V_{\text{th}} = 620\ \text{V}_{\text{rms}}$. For above-threshold motion in one desired location and stationary conditions elsewhere, the 2-D multiplexing inequality $V_{\text{th}}/2 < V_0 < V_{\text{th}}$ must be obeyed for the applied voltage $V_0$. This gives $V_{\text{th}}/75 < V_{\text{in}} < 2V_{\text{th}}/75$ for the input voltage $V_{\text{in}}$. An input voltage of $V_{\text{in}} = 8.3\ \text{V}_{\text{rms}}$ is selected, giving an applied voltage of $V_0 = 310\ \text{V}_{\text{rms}}$. Multiplexed actuation is shown in Fig. 2(a) and 2(b). Microdrop 1 is centered at $i = 6$, $j = 5$, and microdrop 2 is centered at $i = 6$, $j = 10$ to create a configuration for which standard cross-referenced actuation along the $i = 6$ row would normally suffer from multi-microdrop interference. Here, the multiplexing with $V_0(0\ \text{deg})$ on $i = 8$ and 9, and $V_0(180\ \text{deg})$ on $j = 11$ and 12 leads to the enhanced electric field at the activated electrode crosspoint and preferential actuation of microdrop 2 to $i = 8.5$, $j = 11.5$. Microdrop 1 remains stationary. Complete 2-D actuation is ultimately achieved across all $14 \times 14 = 196$ grid points in this multiplexed structure with only $14 + 14 = 28$ inputs.

$V_{\text{th}} = 48\ \text{V}_{\text{rms}}$For practical application to on-chip systems, and primary relevance to biofluidic devices,[29–31] there exists a desire for low input voltages. The above input voltage of $V = 8.3\ \text{V}_{\text{rms}}$ in particular is too large for integration with TTL/CMOS,[16,32] so a device redesign is applied to lower the input voltage. Such lower voltage operation must be considered carefully, though, as the threshold voltage must be pronounced for multiplexed operation. Threshold voltages have been rigorously characterized for voltages down to 50 V,[26] although few analyses exist at lower voltages. With this in mind, a revised digital microfluidic multiplexer is created with identical dimensions to the prior multiplexer and a reduced PDMS layer thickness (1 $\mu$m). The new multiplexer is tested and found have a threshold voltage of $V_{\text{th}} = 48\ \text{V}_{\text{rms}}$. The input voltage operational range of $0.64\ \text{V}_{\text{rms}} < V_{\text{in}} < 1.28\ \text{V}_{\text{rms}}$ for this device is therefore well within the range needed for low-voltage TTL/CMOS operation.

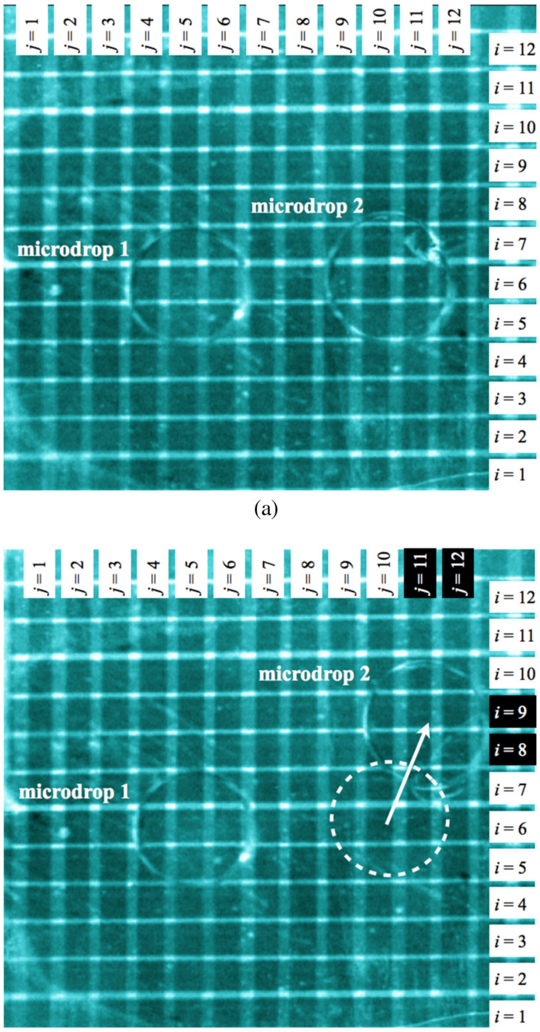

(a)

(b)

**Fig. 2** Digital microfluidic multiplexer operation is shown for a structure with a high threshold voltage, $V_{\text{th}} = 620\ \text{V}_{\text{rms}}$. Microdrop actuation is demonstrated by the (a) initial and (b) final states for motion of microdrop 2 while microdrop 1 is stationary.

Microdrop actuation is shown in Fig. 3 for a selected input voltage of $V_{\text{in}} = 0.64\ \text{V}_{\text{rms}}$. The initial configuration in Fig. 3(a) has microdrop 1 centered at $i = 7.5$, $j = 8$ and microdrop 2 centered at $i = 4.5$, $j = 12.5$. A simple motion algorithm is tested first through voltage activation in two separate steps with the final result shown in Fig. 3(b). In the first step, row $i = 11$ and columns $j = 12$ and 13 are activated to draw microdrop 1 to the $i = 10.5$, $j = 12.5$ crosspoint. In the second step, row $i = 2$ and columns $j = 12$ and 13 are activated to draw

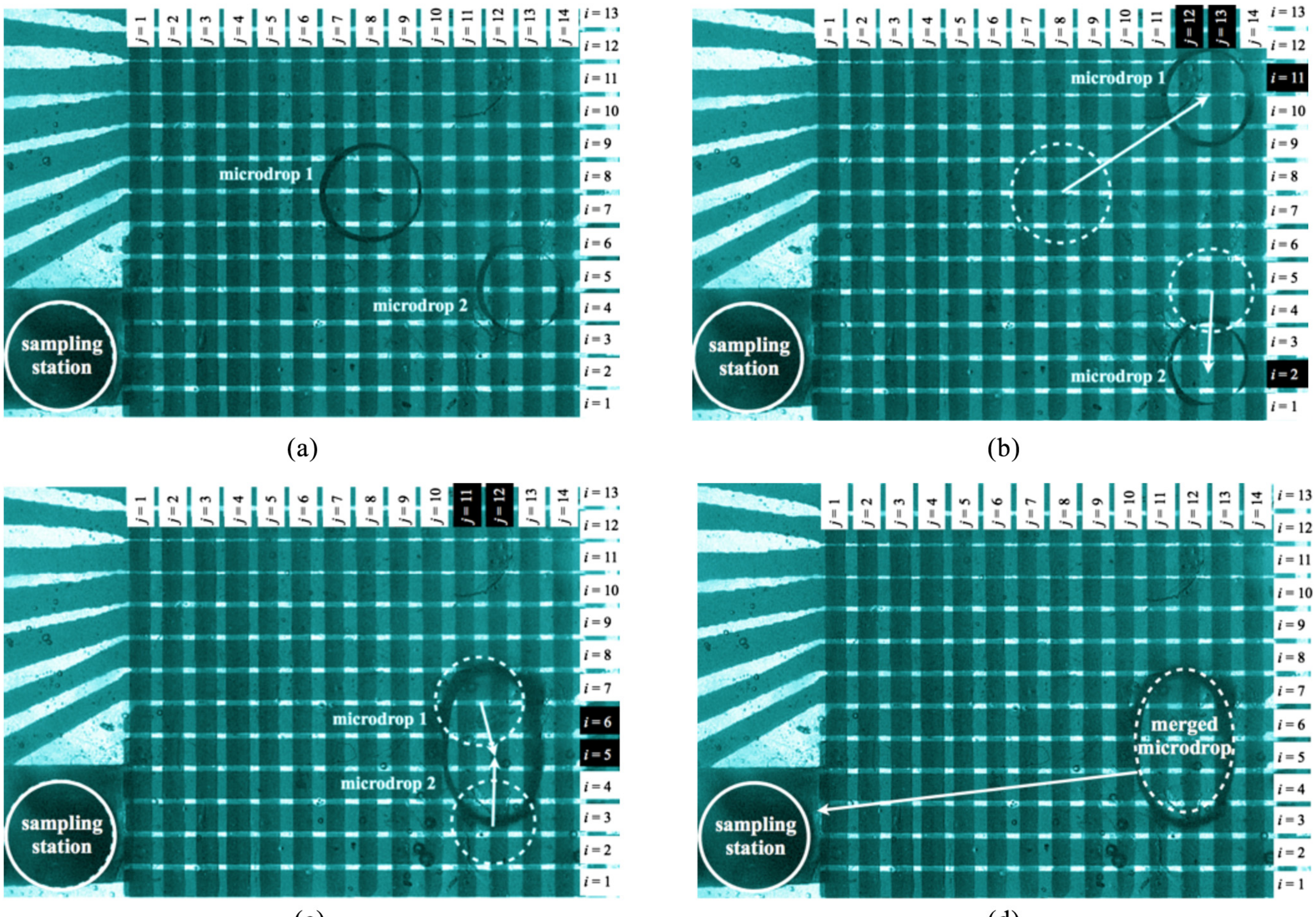

(a) (b) (c) (d)

**Fig. 3** Digital microfluidic multiplexer operation is shown for a structure with low threshold voltage, $V_{\mathrm{th}} = 48\ \mathrm{V_{rms}}$. Microdrop actuation is shown by (a) the initial step, (b) a simple motion algorithm, (c) a more complex mixing algorithm, and (d) moving the merged microdrop to the sampling station.

microdrop 2 to the $i = 2.5$, $j = 12.5$ crosspoint. A second and more complex algorithm is shown in Fig. 3(c) for microdrop mixing. Microdrop 1 and 2 are first drawn together with microdrop 1 pulled to the $i = 6.5$, $j = 11.5$ crosspoint and microdrop 2 pulled to the $i = 2.5$, $j = 11.5$ crosspoint (shown as dashed circles), then the voltage is applied to rows $i = 5$ and 6 and columns $j = 12$ and 13 to draw the microdrops together. A variety of sequences can be ultimately carried out for 2-D multiplexed actuation with this low input voltage, and the complete motion is shown in Fig. 3(c). A final actuation step is used to draw the microdrop of interest to the sampling station in Fig. 3(d) for the optical fluid sensing process of relevance to the following section.

## 3 Sensing

On-chip microfluidic sensing is often implemented through capacitance sampling[33] or optical beam interrogation.[34] Capacitance sampling probes low-frequency dielectric properties through a relationship between the sampled fluid's dielectric constant and the measured capacitance. Unfortunately, capacitance quantities scale down with desired sampling area–diminishing from 75 fF for millimeter-scale droplets to 15 fF for 100 micron-scale[35] droplets—and thus have diminishing measurement potential for smaller device dimensions. Similarly, standard optical beam interrogation, utilizing Fresnel reflection from differing refractive indices, shows diminishing optical signal powers as the sampling cross-sectional area is reduced. Reflected optical powers can become unacceptably low with small device dimensions.

The localized sensing challenges are approached in this investigation with our introduction of a folded-cavity refractive index sensor. Refractometry is performed by the sensor in a manner that maintains linearity between the back-reflected optical beam intensity and internal fluid refractive index. Such an element can be scaled down to smaller device dimensions without sacrificing optical signal intensity. A schematic side-view of the folded-cavity refractive index sensor is shown in Fig. 4(a) and 4(b) with relevant light rays. This optical sensor is implemented as a dedicated sampling station adjacent to the digital microfluidic multiplexer and makes use of the bi-layered form. The overhead microlens must be designed according to the multiplexer dimensions to allow incident collimated beams to converge, reflect off the lower plate surface, focus at an intermediate plane prior to exiting the microlens, and be imaged on the overhead camera image sensor. For localized refractometry measurements, the imaged intensity must show a linear relationship with an appropriate level of sensitivity between the back-reflected beam's intensity and the central fluid refractive index.

For a central fluid layer with a refractive index of $n_f = 1.52$, the ray-tracing results of Fig. 4(a) show a back-reflected beam focusing on the image sensor with a localized high intensity

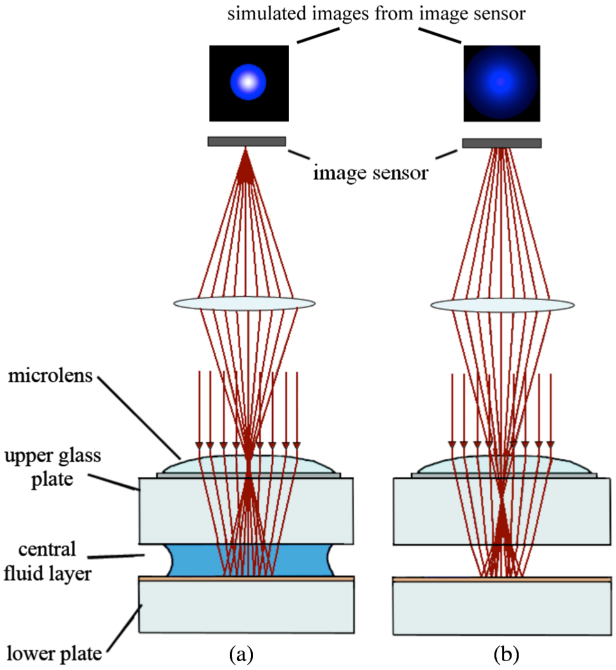

**Fig. 4** The folded-cavity optical sensing system is shown by way of theoretical ray-tracing for (a) a central fluid layer with $n_f = 1.52$ and (b) an air layer with $n_f = 1.00$ between the upper and lower plates. Simulated images are shown above the image sensor for each case.

beam spot. For a central fluid with a refractive index of $n_f = 1.00$, corresponding to air, the ray-tracing results of Fig. 4(b) show a defocused back-reflected beam on the image sensor with a diminished intensity. Given appropriate focal conditions for the microlens, a noticeable contrast can be seen between the imaged optical intensities for a distinct range of internal fluid refractive indices.

The microlens cross-sectional profile defines the relationship between the back-reflected beam intensity on the image sensor and the internal fluid refractive index. A microlens with a high contact angle on the upper glass plate will focus rapidly with a narrow depth of focus, such that small internal fluid refractive index perturbations cause significant changes to the measured intensity, while a microlens with a low contact angle on the upper glass plate will have a long depth of focus, resulting in a reduced sensitivity between the measured intensity and internal fluid refractive index.[36] These relationships become apparent in Fig. 5(a)–5(c). Figure 5(a) shows the image sensor back-reflected beam intensity on the optical axis (OA) for a microlens with a radius of 900 $\mu$m, a height of 660 $\mu$m, and a contact angle of $\theta = 72.5$ deg. A narrow refractive index range of $n_f = 1.492$ to 1.500 is shown as the range over which the intensity varies by 20% and is linearly related to $n_f$ by way of $I_{\mathrm{OA}}(n_f) = 24.13n_f - 35.202$ (with an $R^2$ value of 0.9965). The depth of focus and refractive index range can be made to increase by reducing the microlens contact angle, and such an increase is apparent in Fig. 5(b) for a microlens with a radius of 900 $\mu$m, a height of 490 $\mu$m, and a contact angle of $\theta = 57.5$ deg. A widened refractive index range of $n_f = 1.45$ to 1.52 establishes the same 20% intensity variations and linear relationship to $n_f$ by way of $I_{\mathrm{OA}}(n_f) = 2.9398n_f - 3.4741$ (with an $R^2$ value of 0.9973). This trend toward increased depth of focus and refractive index range continues in the results of Fig. 5(c), for a microlens with a radius of 900 $\mu$m, a height of 350 $\mu$m, and a contact angle of $\theta = 42.5$ deg. An especially wide refractive index range of $n_f = 1.28$ to 1.52 facilitates an intensity variation of 20% according to the linear relationship: $I_{\mathrm{OA}}(n_f) = 0.8145n_f - 0.2396$ (with an $R^2$ value of 0.9999). Microlens contact angles, $\theta = 42.5$ deg, 50.0 deg, 57.5 deg, 65.0 deg, 72.5 deg, and 80.0 deg, and their corresponding linear refractive index sensing ranges are listed in Table 1.

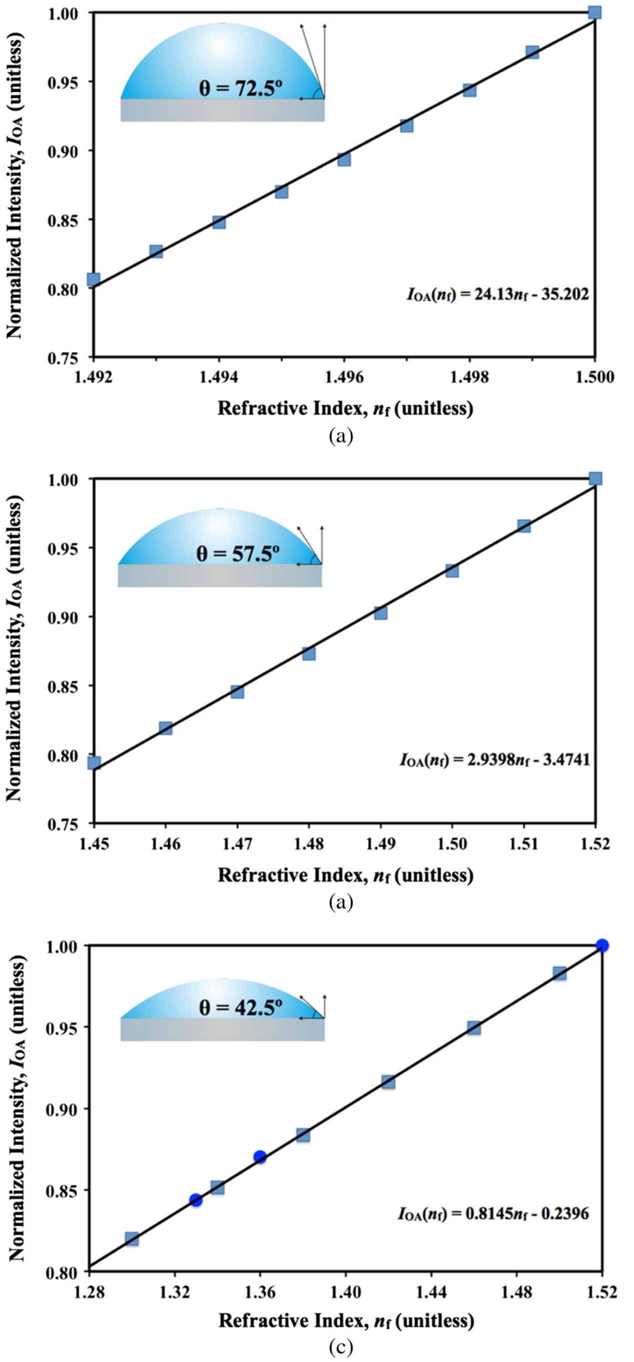

**Fig. 5** Normalized optical axis (OA) intensities are shown as a function of the fluid refractive index $n_f$. Theoretical results are shown as solid squares in (a) and (b) for microlens contact angles of 72.5 deg and 57.5 deg respectively. Theoretical and experimental results are shown in (c) as solid squares and circles, respectively, for a microlens contact angle of 42.5 deg. The corresponding microlens profiles and linear equations are shown as insets with the linear expressions plotted as solid lines.

**Table 1** Microlens contact angles are shown with their corresponding fluid refractive index ranges for linear optical sensing.

| $\theta$ (°) | $n_f$ range |
|---|---|
| 42.5 | 1.28 to 1.52 |
| 50.0 | 1.36 to 1.52 |
| 57.5 | 1.45 to 1.52 |
| 65.0 | 1.47 to 1.52 |
| 72.5 | 1.492 to 1.500 |
| 80.0 | 1.495 to 1.500 |

The above-mentioned relationships between the back-reflected image OA intensities and internal fluid refractive indices are ultimately prescribed by way of microlens contact angles. A lower contact angle can be applied if operation is desired over a wide refractive index range in, for example, discriminating distinct fluids in a digital microfluidic system. A larger contact angle can be applied if high-sensitivity operation is desired over a narrow refractive index range in, for example, optical sampling of chemical kinetics[37] and temperature characteristics.[38] In terms of error and uncertainty, high-sensitivity measurements must also carefully control the environmental conditions—temperature instability of 1°C can result in refractive index fluctuations on the order of 0.0005.[38]

An in-situ and adaptable polymer deposition process, electro-dispensing,[20] is employed for the required microlens contact angle tuning. The electro-dispensing technique shown in Fig. 6 forms the microlens above the sampling station by dispensing of a UV-curable polymer droplet with a voltage-activated metal dispensing tip. The dispensed droplet profile is defined by both nominal polymer surface tensions and the localized electric field formed between the metal dispensing tip voltage, $V_{\rm disp}$, and a lower grounded copper plate. The electrocapillary response of the microlens droplet is dictated by way of the Lippmann-Young equation,[39]

$$\cos\,\theta(V_{\rm disp}) = \cos\,\theta + \frac{cV_{\rm disp}^2}{2\gamma_{lf}} = \frac{\gamma_{sf}-\gamma_{sl}}{\gamma_{lf}} + \frac{cV_{\rm disp}^2}{2\gamma_{lf}}, \qquad (2)$$

where $c$ is again the capacitance per unit area. Initial conditions with $V_{\rm disp} = 0$ define the nominal contact angle $\theta_0$, with $\gamma_{sf}$, $\gamma_{sl}$ and $\gamma_{lf}$ as the solid-filler, solid-liquid, and liquid-filler surface tensions, respectively. Voltage-activated conditions with $V_{\rm disp} \neq 0$ define the user-controlled modified contact angle $\theta(V_{\rm disp})$. With a surrounding air filler and appropriate substrate, the polymer microlens can be given a sufficiently high nominal contact angle, $\theta_0$, and the electro-dispensing tip voltage $V_{\rm disp}$ can be used to lower the contact angle, prior to UV-curing, and tune it to the desired focusing conditions.

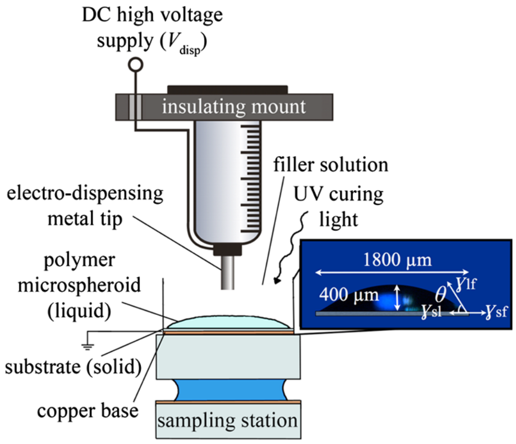

**Fig. 6** Optical tuning of the microlens contact angle, and therefore the refractive index operational range, is brought about through the electro-dispensing system shown here.

To facilitate localized optical sensing of fluid refractive indices between the upper and lower multiplexer plates, a folded-cavity refractive index sensor is incorporated as a sampling station adjacent to the multiplexer. This sampling station is shown in the bottom left of all Fig. 3 photographs. A collimated white light LED illuminates the structure, and the returned optical beam is sampled by a beamsplitter and camera image sensor. Fluid samples are pulled into the sampling station, as shown in Fig. 3(d), by activating the appropriate electrode series and images are captured.

The microlens used in the experimental device is fabricated utilizing the afore-mentioned electro-dispensing technique to establish well-controlled focusing conditions. Norland Optical Adhesive (NOA) 68 UV-curable polymer is dispensed as the microlens on a PTFE-coated glass substrate. The desired microlens radius of 900 $\mu$m is defined by dispensing the polymer with a pressure-controlled dispenser (Nordson Ultimus V), giving highly reproducible microlens volumes. The dispensing tip voltage is then tuned across the range of $V_{\rm disp} = 300$ $\rm V_{DC}$ to 1500 $\rm V_{DC}$, and a contact angle of 42.5 deg is selected for curing and subsequent testing. This microlens profile is chosen to facilitate testing over a wide range of fluid refractive indices. Fluids with well-known refractive indices are selected for this calibration test: water ($n_f = 1.33$), ethanol ($n_f = 1.36$), and silicone oil ($n_f = 1.52$). Figure 5(c) shows the resulting measured intensity as a linear function of fluid refractive indices. Measurement uncertainty in the apparatus is quantified by an intensity error of 1% and a corresponding refractive index uncertainty of 0.01 for this wide-range and low-sensitivity configuration. If enhanced sensitivities with lower refractive index uncertainties are desired over narrower refractive index ranges, the afore-mentioned large contact angle microlenses can be employed. Overall, the optical probing characteristics of the optical sampling system are found to accurately characterize a variety of internal fluid refractive indices within the chip.

## 4 Conclusions

The demonstrated work introduced microdrop actuation and sensing implementations that are well-suited to localized on-chip operation. A digital microfluidic multiplexer was presented as an architecture that provides complete 2-D microdrop motion in a system with decreased input complexity and input voltages compatible with TTL/CMOS technologies. At the same time, an optical sampling station with a folded-cavity arrangement was fabricated and demonstrated for the sampling of internal fluid refractive indices. The microlens system was designed and characterized to establish the desired relationship between the back-reflected intensity and fluid refractive index. It was found that user-defined refractive index ranges and sensitivities can be obtained by tuning of the microlens contact angle. Overall, issues of digital microfluidic device scalability were addressed for both actuation and sensing in the demonstrated work, and the resulting system can be successfully applied in the integrated technologies of future lab-on-a-chip devices.

## References

1. H.-C. Lin, Y.-J. Liu, and D.-J. Yao, "DNA litigation using coplanar electrodes electro-wetting-on-dielectric (EWOD) device," in *Proc. 4th IEEE Int. Conf. Nano/Micro Engineered and Molecular Systems*, pp. 385–389, IEEE Computer Society, Washington, DC, USA (2009).
2. T. H. Schulte, R. L. Bardell, and B. H. Weigl, "Microfluidic technologies in clinical diagnostics," *Clin. Chem. Acta* **321**(1–2), 1–10 (2002).
3. C. Neils et al., "Combinatorial mixing of microfluidic streams," *Lab Chip* **4**(4), 342–350 (2004).
4. M. Brivio, W. Verbroom, and D. N. Reinhoudt, "Miniaturized continuous flow reaction vessels: influence on chemical reactions," *Lab Chip* **6**(3), 329–244 (2006).
5. J. P. Urbanski et al., "Digital microfluidics using soft lithography," *Lab Chip* **6**(1), 96–104 (2006).
6. J. Lee et al., "Electrowetting and electrowetting-on-dielectric for microscale liquid handling," *Sensor. Actuator A* **95**(2), 259–268 (2002).
7. T. Xu et al., "Automated design on pin-constrained digital microfluidic biochips under droplet-interference constraints," *ACM J. Emerg. Tech.* **3**(3), 14:1–14:23 (2007).
8. V. Srinivasan, V. K. Pamula, and R. B. Fair, "An integrated digital microfluidic lab-on-a-chip for clinical diagnostics on human physiological fluids," *Lab Chip* **4**(4), 310–315 (2004).
9. M. G. Pollack, R. B. Fair, and A. D. Shenderov, "Electrowetting-based actuation of liquid droplets for microfluidic applications," *Appl. Phys. Lett.* **77**(11), 1725–1726 (2000).
10. K. Bohringer, "Modeling and controlling parallel tasks in droplet-based microfluidic systems," *IEEE Trans. CAD* **25**(2), 329–339 (2006).
11. J. Berthier, *Microdrops and Digital Microfluidics*, William Andrew Inc., Norwhich, NY (2008).
12. M. J. Jebrail and A. R. Wheeler, "Let's get digital: digitizing chemical biology with microfluidics," *Curr. Opin. Chem. Biol.* **14**(5), 574–581 (2010).
13. P. Paik, V. K. Pamula, and R. B. Fair, "Rapid droplet mixers for digital microfluidic systems," *Lab Chip* **3**(4), 253–259 (2003).
14. J. Gong and C.-J. Kim, "Direct-referencing two-dimensional-array digital microfluidics using multi-layer printed circuit board," *J. MEMS* **17**(2), 257–264 (2008).
15. C. M. Collier et al., "Nonlinear dual-phase multiplexing in digital microfluidic architectures," *Micromachines* **2**(4), 369–384 (2011).
16. Y. Li et al., "Anodic $Ta_2O_5$ for CMOS compatible low voltage electrowetting-on-dielectric device fabrication," *Solid-State Electron.* **52**(9), 1382–1387 (2008).
17. M. J. Madou and R. Cubicciotti, "Scaling issues in chemical and biological sensors," *Proc. IEEE* **91**(6), 830–838 (2003).
18. A. Ahmadi et al., "In situ characterization of microdroplet interfacial properties in digital microfluidic systems," *Lab Chip* **10**(11), 1429–1435 (2010).
19. M. Han, F. Guo, and Y. Lu, "Optical fiber refractometer based on cladding-mode Bragg grating," *Opt. Lett.* **35**(3), 399–401 (2010).
20. B. Born, E. L. Landry, and J. F. Holzman, "Electro-dispensing of micro-spheroids for lateral refractive and reflective photonic elements," *IEEE Photon. J.* **2**(6), 873–883 (2010).
21. E. Maftei, P. Pop, and J. Madsen, "Tabu search-based synthesis of digital microfluidic biochips with dynamically reconfigurable non-rectangular devices," *Des. Autom. Embed. Syst.* **14**(3), 287–307 (2010).
22. D. Davids et al., "Multiple fault diagnosis in digital microfluidic biochips," *ACM J. Emerg. Tech.* **2**(4), 262–276 (2006).
23. Z. Xiao and E. F. Young, "CrossRouter: a droplet router for cross-referencing digital microfluidic biochips," in *Proc. 15th Asia South Pacific Design Automation Conf.*, pp. 269–274, IEEE Press, Piscataway, NJ, USA (2010).
24. M. Cho and D. Z. Pan, "A high-performance droplet routing algorithm for digital microfluidic biochips," *IEEE Trans. Comput. Aided Des.* **27**(10), 1714–1724 (2008).
25. T. Zhu and K. Chakrabarty, "A droplet-manipulation method for achieving high-throughput in cross-referencing-based digital microfluidic biochips," *IEEE Trans. Comput. Aided Des.* **27**(11), 1905–1917 (2008).
26. R. Renaudot et al., "Optimization of liquid dielectrophoresis (LDEP) digital microfluidic transduction for biomedical applications," *Micromachines* **2**(2), 258–273 (2011).
27. A. Dolatabadi, K. Mohseni, and A. Arzpeyma, "Behaviour of a moving droplet under electrowetting actuation: numerical simulation," *Can. J. Chem. Eng.* **84**(1), 17–21 (2006).
28. F. Su, W. Hwang, and K. Chakrabarty, "Droplet routing in the synthesis of digital microfluidic biochips," in *Proc. Des. Autom. Test Eur.*, Munich, Germany, pp. 323–328 (March 6–10 2006).
29. C.-T. Ho et al., "Micromachined electrochemical T-switches for cell sorting applications," *Lab Chip* **5**(11), 1248–1258 (2005).
30. A. P. Chandrakasan, N. Verma, and D. C. Daly, "Ultralow-power electronics for biomedical applications," *Annu. Rev. Biomed. Eng.* **10**(1), 247–274 (2008).
31. R. H. W. Lam, M.-C. Kim, and T. Thorsen, "Culturing aerobic and anaerobic bacteria and mammalian cells with a microfluidic differential oxygenator," *Anal. Chem.* **81**(14), 5918–5924 (2009).
32. H. Moon et al., "Low voltage electrowetting-on-dielectric," *J. Appl. Phys.* **92**(7), 4080–4087 (2002).
33. A. Ahmadi et al., "Digital implementations for integrated microfluidic sensing," *Proc. SPIE* **7318**, 73181C (2009).
34. C. Monat, P. Domachuk, and B. J. Eggleton, "Integrated optofluidics: a new river of light," *Nat. Photon.* **1**(2), 106–114 (2007).
35. C. Elbuken et al., "Detection of microdroplet size and speed using capacitive sensors," *Sensor Actuator A* **171**(2), 55–62 (2011).
36. J. L. Cruz-Campa et al., "Microlens rapid prototyping technique with capability for wide variation in lens diameter and focal length," *Microelectron. Eng.* **87**(11), 2376–2381 (2010).
37. G. Ladam et al., "Protein adsorption onto auto-assembled polyelectrolyte films," *Langmuir* **17**(2–6), 878–882 (2001).
38. W. B. Li et al., "Determination of the temperature and concentration dependence of the refractive index of a liquid mixture," *J. Chem. Phys.* **101**(6), 5058–5069 (1994).
39. F. Mugele and J. C. Baret, "Electrowetting: from basics to applications," *J. Phys.: Condens. Matter* **17**(28), R705–R774 (2005).